Multiscale Modeling of the Ultrafast Electron Microscope: From the Photocathode to the Sample

J. Portman, H. Zhang, K. Makino, C.-Y. Ruan, M. Berz, P.M. Duxbury
Michigan State University, Michigan, USA

Abstract

By modeling the photoemission process of high-brightness electron beams, we investigate the role of laser fluence and extraction field, as well as virtual cathode physics and the limits to spatiotemporal and spectroscopic resolution originating from the aspect ratio of the exciting laser pulse. We also provide a comparison of our model with experimental images of the photoemission process. We then present our development of a design for the ultrafast electron microscope (UEM) column using the analytic Gaussian model and calculate the achievable temporal and spatial resolutions under different photoemission conditions.

Keywords: Ultrafast electron microscope (UEM), photoemission, analytic Gaussian model

1. INTRODUCTION

The invention and spread of commercially available femtosecond lasers has opened the door for the study of ultrafast nonequilibrium processes in materials, and this field has grown rapidly over the last decade. The term *ultrafast* generally indicates phenomena that take place on ns (10^{-9} s) or faster timescales and, correspondingly, on length scales between μm (10^{-6} m) and Å (10^{-10} m). This broad class spans the fields of biology (Zewail, 2010), material science from ultrafast phase transitions (Ruan et al., 2004) to charge transport at nanointerfaces (Ruan et al., 2009) and dynamics in correlated electron materials (Tao et al., 2012a), chemistry (Zewail, 2000; Nicodemus et al., 2011), and plasma physics (Hau-Riege et al., 2012).

In practice, these systems are best explored by using the well-known pump-probe technique: the sample under consideration is excited by the pump pulse, and its response at various delay times is measured with a probe pulse. By recording the response of the system as a function of delay time, we can obtain a description of its time evolution, provided that both the pump and the probe pulse have sufficient time resolution. While femtosecond lasers have become the tool of choice as pump pulses, the main candidates

for probing the structural response are X-rays and electrons (King et al., 2005; Carbone et al., 2012). X-rays offer angstrom-size wavelengths, high spatial coherence, and short pulse length, but their generation with a high-enough brightness requires large-scale facilities. Electron probes, on the other hand, are easily generated using tabletop scale equipment, inflict less damage on the sample than do X-rays, and have a high-scattering cross section. The drawback is that using a charged particle beam leads to defocusing due to the Coulomb repulsion. Understanding the extent to which this space charge broadening between the electrons can be compensated for by using magnetic lenses and RF cavities is still an open question (Tao et al., 2012; van Oudheusden et al., 2010; Li & Musumeci, 2014).

The focus of this paper is to present an overview of the theoretical work done to guide the development of the ultrafast electron microscope (UEM) system at Michigan State University. In the next section, the photoemission process of high-brightness electron beams is analyzed in detail and optimal pulse generation conditions are discussed, while section 3 focuses on incorporating these results into a mean field model describing the whole microscope column to provide estimates of the achievable resolution in the system for various photoemission conditions. Section 4 offers a brief conclusion.

2. GENERATION OF THE ELECTRON PULSE

The initial photoemission stage is critical for the operation of the UEM as the phase space volume occupied by the pulse sets limits on the achievable temporal and spatial resolutions and depends on the extraction conditions and the initial Coulomb expansion. For this reason, it is necessary to minimize the increase in beam emittance due to space charge effects while maintaining a high number of electrons. Another issue to take into account is the so called virtual cathode (VC) limit, in which the negative charge of the electrons emitted at earlier times, combined with the attractive surface field, hinders further emission of particles and causes a degradation of the pulse properties. To better understand the nonlinear interplay between the space charge driven expansion, laser properties, photocathode material properties, and virtual cathode physics, we have conducted explicit N-particle simulations of the electron photoemission process using COSY INFINITY, a code designed for high-performance scientific computing and beam dynamics simulations (Makino & Berz, 2006).

The electron bunch is generated through photoemission from a gold photocathode irradiated with a laser pulse. This process can be described using the so-called three-step photoemission model (Berglund & Spicer, 1964; Dowell & Schmerge, 2009) in which each electron is emitted independently as a result of absorbing a photon of energy $\hbar\omega$, diffusing to the surface and escaping to the vacuum. The initial velocities are calculated taking into account that in order to escape the photocathode, the electrons need to overcome the work function of the material. Taking z as the direction perpendicular to the photocathode surface, the following equations result for the initial velocities:

$$v_{x\,out} = v\sin\theta\cos\phi, \tag{1}$$

$$v_{y\,out} = v\sin\theta\sin\phi, \tag{2}$$

$$v_{z\,out} = \sqrt{(v\cos\theta)^2 - 2(E_F + W)/m_0}, \tag{3}$$

where $v = \sqrt{\frac{2(E_i + \hbar\omega)}{m_0}}$, E_i is the randomly generated initial energy of the electron, E_F is the photocathode Fermi energy, W is its work function, m_0 is the electron rest mass, and $\hbar\omega$ is the laser pulse energy. $\theta \in [0, \theta_{max}]$ and $\phi \in [0, 2\pi]$. θ_{max} is the maximum angle for which the electron can escape with sufficient velocity in the z direction and is given by

$$\cos\theta_{max} = \frac{v_{z\,min}}{v} = \sqrt{\frac{E_F + W}{E_i + \hbar\omega}}. \tag{4}$$

The initial coordinates in directions parallel to the surface (x, y in our notation) are randomly generated given the spatial profile of the laser pulse, and the initial z coordinate is set equal to zero. The time evolution of the emitted electrons is treated by solving their relativistic equations of motion at each time step using a fourth-order Runge-Kutta algorithm. The particles that fall back on the surface ($z < 0$) are removed from the simulation and collisions between electrons are avoided by imposing a maximum force cut-off. The Coulomb forces felt by the electrons are treated through a multiple-level fast multipole method (MLFMM) (Zhang & Berz, 2011; Zhang, 2013), and we use macroparticles to further reduce the computational time and allow simulations with higher numbers of electrons. A more in-depth description of the MLFMM can also be found in Zhang et al. (2015). In addition to the external extraction field F_a, we include the effect of the image charge field generated by the electrons on the cathode surface. Further

details on our implementation can be found in Portman et al. (2013, 2014) and Portman (2014).

Comparing the time-dependent longitudinal density profiles of photoemitted electron bunches extracted from shadow imaging experiments [Figure 1(A), circles at 50 and 80 ps] (Tao et al., 2012) with the simulations under the same conditions (red lines), we observe excellent agreement for the description of the front of the beam. The shaded regions in the figure indicate portions of the beam close to the surface where the charge density is not fully accessible experimentally due to strong surface scattering of the probe beam. Overall, our model accurately captures the propagation of the pulse over tens of picoseconds, indicating that the relevant physics of the process is correctly described.

Experimental data on the longitudinal pulse width σ_z indicated a universal sublinear scaling with the number of electrons N_e^{emit} [Figure 1(B)]. Our simulations show that this is somewhat accidental as it is a result of the linear growth of σ_z in the sub-virtual cathode regime at low values of N_e^{emit} combined with its reduced increase as the VC regime sets in.

In order to use the generated electron bunch for single-shot imaging or diffraction, we require between 10^5 and 10^9 electrons per pulse, so another key quantity of interest is the final number of electrons at the end of the photoemission process. This is shown in Figure 1(C) as a function of the initial number of electrons, N_e^0 for varying extraction fields F_a. For a low number of generated electrons ($N_e < 10^6$), all of the particles escape the surface, creating the linear relationship seen in the first part of the figure. As the initial number of electrons is increased, the space charge effect also increases due to both the electrons and the image charge on the surface until the VC limit is reached.

Increasing the extraction field shifts the onset of this phenomenon, enabling the emission of a higher number of particles from the photocathode. The critical value of extracted charge corresponding to the onset of the VC is plotted in the inset of Figure 1(C) as a function of extraction field F_a, with the dashed line indicating a fit to the analytical model presented in Valfells et al. (2002). This model approximates the pulse as a sheet of charge to derive an equation for the critical charge density in the transverse direction [see Eqs. (3) and (7) in Valfells et al. (2002)]: $\rho_{q,crit} = N_e^{crit}/\left(\pi\sigma_r^2\right) = \epsilon_0 F_a$, where σ_r is the width of the pulse and ϵ_0 is the dielectric permittivity.

To better understand the microscopic dynamics leading to virtual cathode formation, we present snapshots of the time evolution of the pulse in the x-z plane in Figure 2 through a color map of the charge distribution of the

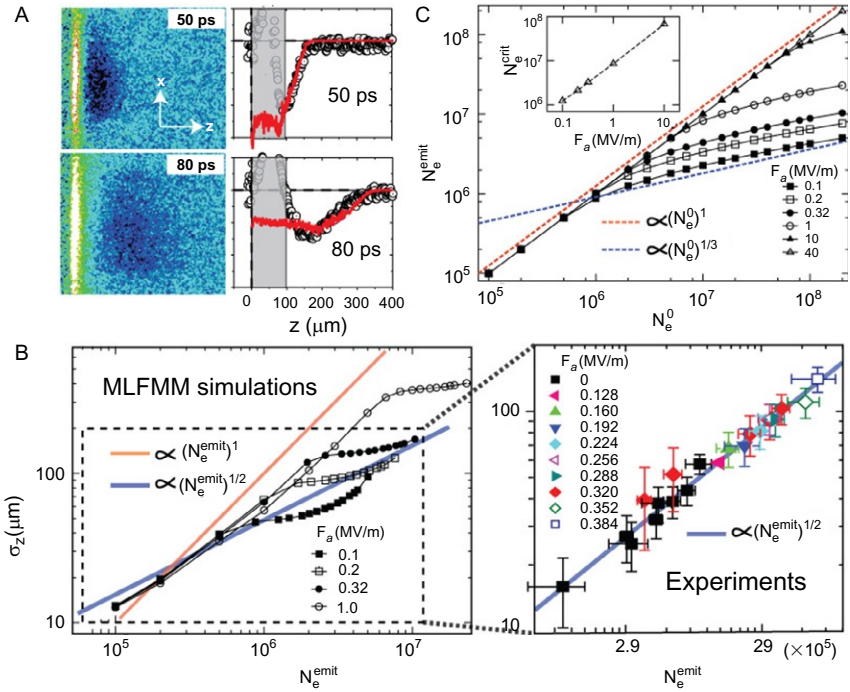

Figure 1 (A) Comparisons of MLFMM simulations of longitudinal charge density profiles (red lines) and data (circles) extracted from the shadow imaging experiments at 50 and 80 ps. (B) Sublinear scaling of longitudinal bunch size σ_z versus number of electrons emitted (N_e^{emit}) taken at 120 ps from MLFMM simulations (left panel), and compared to the shadow imaging data (right panel). (C) N_e^{emit} versus the number of generated electrons (N_e^0) for various extraction fields (F_a), showing evidence of virtual cathode formation. Inset: Threshold number of electrons (N_e^{crit}) for virtual cathode formation as a function of F_a (*Reprinted with permission from Portman et al., 2013; Copyright 2013, AIP Publishing LLC.*).

bunch overlaid with arrows representing the average electron velocity. Also shown are projections of the density onto the x- and z-axes. For short timescales, the spatial profile of the pulse retains the Gaussian distribution of the generating laser pulse [Figure 2(A)]. The velocities show a turbulent flow related to the initial thermal distribution from which they were generated and independent of extraction field. At later times, the pulse begins to move away from the surface, and for conditions below the virtual cathode limit, the flow becomes fully laminar [Figure 2(B)]. The pulse evolves into the typical pancake shape, with an ellipsoidal transverse profile and a sharp peak corresponding to the center of the pancake in the longitudinal direction. On the other hand, above the VC limit [Figure 2(C)], the pulse retains some

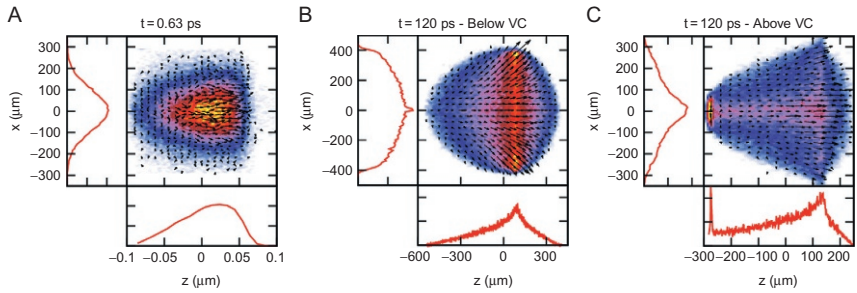

Figure 2 Color map of the charge distribution in the rest frame of the bunch projected onto the *x*-*z* plane, overlaid with arrows representing the average electron velocity and projected onto the *x*- and *z*-axes. (A) Initial stage of photoemission, which is independent of extraction field. (B), (C) Final stage at $t = 120$ ps for conditions below and above the virtual cathode limit for $N_e^0 = 7 \cdot 10^6$ and extraction fields $F_a = 10$MV/m and $F_a = 0.32$MV/m, respectively.

turbulent flow and does not fully detach from the surface. In the transverse direction, it presents a superposition of ellipsoidal and Gaussian components, while in the longitudinal (z) direction, we observe a peak in the density for values of z close to the surface, which is a typical signature of the virtual cathode limit.

To compare different regimes of pulse generation and find optimal photoemission conditions, both the transverse and longitudinal emittances are of importance as they determine, respectively, the spatial and temporal resolutions achievable. Ideal pulse generation conditions would minimize both the longitudinal (z) and transverse (x) normalized emittances, defined as (Luiten et al., 2004)

$$\epsilon_x = \frac{1}{m_0 c}\sqrt{\langle x^2\rangle\langle p_x^2\rangle - \langle x p_x\rangle^2}. \tag{5}$$

It is worth noting here that the quantity ϵ_x defined in Eq. (5) is a statistical approximation of the true 6D emittance, and it assumes that there is little correlation between the x-, y- and z-directions so that the dynamics decouples into three independent 2D cases. We calculate this quantity and parameters derived from it, as traditionally the emittance has been used as a key figure of merit for UEM systems since it provides an easily accessible estimate of the phase space occupied by the pulse (Portman et al., 2013).

When comparing different photoemission conditions, it is also necessary to take into account the aspect ratio of the laser pulse. Our discussion so far has presented results relative to the so-called pancake regime, characterized

by a laser pulse in which the transverse width is greater than the longitudinal one ($\sigma_r \gg \sigma_z$). The cigar regime on the other hand is characterized by an elongated pulse in which $\sigma_z \gg \sigma_r$, and this has been suggested (Filippetto et al., 2014) as a promising choice to improve the extraction efficiency by shifting the onset of the VC at the expense of the temporal resolution.

As shown in Figure 3(A), varying the aspect ratio of the exciting laser pulse from pancake to cigar-like leads to a decrease in the transverse emittance at the expense of an increase in the longitudinal component. Extraction of pulses with a higher charge causes a strong increase in the longitudinal (transverse) emittance for the pancake- (cigar-) shaped pulses, respectively. This can be compensated to some extent by increasing the extraction field F_a. From this, we conclude that for applications requiring both temporal and spatial resolutions, a pancake-like pulse may be more appropriate. On the other hand, if time resolution is not essential and a higher longitudinal emittance is acceptable, one can obtain increased spatial resolution by using an elongated, cigar-like photoemitting laser pulse.

In addition to the emittance, our ability to resolve spatial features can be quantified with the coherence length L_c, which at the beam waist can be expressed as (van Oudheusden et al., 2007)

$$L_c = \frac{h}{2m_0 c}\frac{\sigma_r}{\epsilon_x}, \tag{6}$$

where, as discussed previously, we have assumed that the transverse and longitudinal directions are decoupled, h is Plank's constant, m_0 is the rest

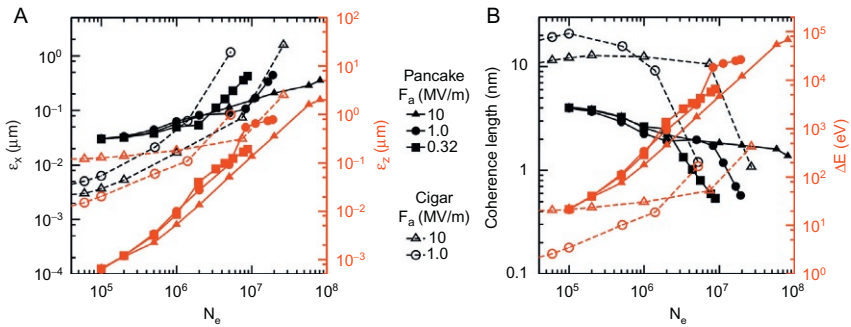

Figure 3 Comparison between pancake-like and cigar-like pulses for increasing values of extraction field F_a and number of electrons in the pulse: (A) transverse (black) and longitudinal emittance (red) and (B) coherence length (black) and energy spread ΔE (red).

mass of the electron, c is the speed of light, σ_r is the beam radius, and ϵ_x is the normalized transverse emittance.

The energy spread, defined as (Portman et al., 2013)

$$\Delta E = \frac{\epsilon_z}{\Delta t} m_0 c, \tag{7}$$

where ϵ_z is the normalized longitudinal emittance and Δt is the temporal resolution, is also a key quantity that should be minimized for optimal operation.

To conclude our discussion, we compare the coherence length and the energy spread for pancake-like and cigar-like pulses in Figure 3(B). The cigar-like pulse presents significantly better coherence length and lower energy spread compared to the pancake-like pulses until the VC limit is reached. As the number of electrons is increased to above the VC, the cigar shape shows a very sharp decrease of the coherence length. In contrast, while the pancake-like pulses display lower coherence lengths and higher energy spreads overall, their dependence on the number of electrons is less critical. Increasing the extraction field F_a significantly increases the energy spread of the cigar-like case while the pancake is unaffected.

3. BUILDING THE ELECTRON MICROSCOPE

During the photoemission process discussed so far, nonlinear effects play a key role in determining the pulse properties. In the first 100 ps, the pulse rapidly expands as a result of the repulsive stochastic Coulomb forces. After this initial stage, the charge density is sufficiently low that a mean field model can be used to describe the dynamics of the electrons inside the microscope. To do so, we adapt the so-called analytic Gaussian model introduced by Michalik and Sipe (2006) and refined by Berger and Schroeder (2010), to be applicable to the UEM system (Portman 2014).

In the analytic Gaussian model, the electron bunch is modeled with a product of Gaussian distributions in both momentum and position:

$$f(\mathbf{r}, \mathbf{p}; t) = C f_T\left(x, y, p_x, p_y; t\right) f_z(z, p_z; t), \tag{8}$$

where

$$f_T\left(x, y, p_x, p_y; t\right) = \exp\left[-\frac{x^2 + y^2}{2\sigma_T} - \frac{\left[p_x - (\gamma_T/\sigma_T)x\right]^2 + \left[p_y - (\gamma_T/\sigma_T)y\right]^2}{2\eta_T}\right], \tag{9}$$

$$f_z(z, p_z; t) = \exp\left[-\frac{z^2}{2\sigma_z} - \frac{[p_z - (\gamma_z/\sigma_z)z]^2}{2\eta_z}\right]. \quad (10)$$

Here, $\sigma_{T,z}$, $\eta_{T,z}$, and $\gamma_{T,z}$ are time-dependent parameters that describe, respectively, the spatial width, kinetic energy spread, and chirp of the electron pulse (Figure 4). Equations of motion are derived for these parameters using a mean-field self-similar approximation. By treating the effect of the various optical elements on the pulse properties, we build a model for the UEM that includes the photoemission gun, magnetic lenses, and RF cavity. The strengths of the lenses and of the electric field in the RF cavity were used as variables in an optimization routine to control the position and spot size of the beam waist. The initial pulse parameters (number of electrons, center of mass velocity and analytic Gaussian parameters) were extracted from the simulations of the photoemission process discussed in the previous section. The emittance is a conserved quantity in this model and its value is also determined from the initial photoemission conditions. For this reason, in simulating the microscope design, we will focus on the optimal achievable bunch size for given photoemission conditions.

Results for the column optimized for $N_e = 10^6$ electrons generated with a pancake-like laser pulse and a kinetic energy of 100 keV are shown in Figure 5, where we plot the longitudinal and transverse bunch sizes as a function of position along the microscope. The beam waist is at ~1090 mm, with pulse size 0.92 μm in the transverse and 2.3 μm in the longitudinal direction. Due to the strength of the lens used to focus the pulse, for positions close to the

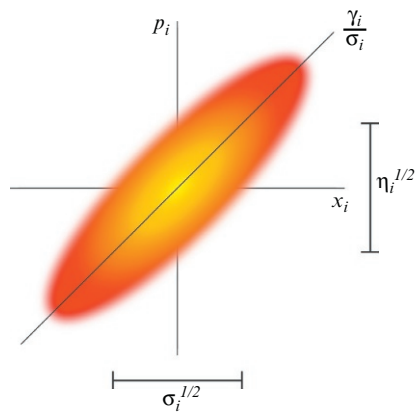

Figure 4 Schematic representation of the pulse parameters used in the analytic Gaussian model in phase space.

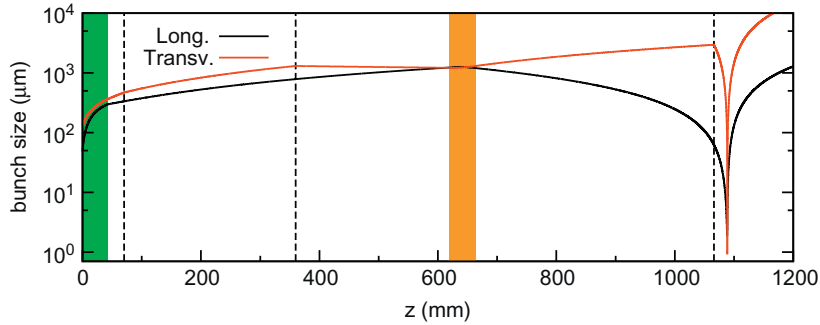

Figure 5 Transverse and longitudinal bunch sizes as a function of position along the column of the UEM. The region corresponding to the photoemission gun is shown in green, while that corresponding to the RF cavity is in yellow. The dashed lines correspond to the magnetic lenses. The electron beam is composed of $N_e = 10^6$ electrons with a kinetic energy of 100 keV emitted with a pancake-like laser pulse with an initial transverse width of 100 μm and a temporal duration of 50 fs.

Table 1 Pulse parameters at the beam waist for a 100-keV electron bunch with varying number of electrons N_e

	Transverse Size (μm)	Transverse emitt. (nm)	Bunch Length (fs)	Energy Spread ($\times 10^{-4}$)
$N_e = 10^5$ Pancake	0.98	27	13	3.7
$N_e = 10^6$ Pancake	0.92	75	40	9.3
$N_e = 10^7$ Pancake	0.94	210	290	24
$N_e = 10^6$ Cigar	0.14	21	420	17
Goal: $N_e > 10^6$	~1–10	<20	<100	<10

The pancake-like pulses are generated with a 50-fs laser beam with a transverse width of 100 μm; for the cigar-like pulse, we used a 10-ps laser with a transverse spot size of 10 μm. The reported goal parameters are taken from (van Oudheusden et al., 2007, Berger et al., 2009, van der Geer et al., 2009, Tao et al., 2012).

beam waist, the transverse width diverges rapidly so that accurate positioning of the sample at the beam waist is crucial for good spatial resolution. The divergence of the longitudinal component is less severe.

We perform similar optimizations varying the number of electrons in the pulse and summarize our results in Table 1. The transverse pulse sizes are comparable for all the simulations reported, which is in part due to the lack

of aberrations in the analytic Gaussian model, which would play a role as the width of the pulse is increased. Also not included in the model are stochastic space charge effects, which would lead to an additional broadening of the pulse at the beam waist due to electron-electron repulsion. In any case, the transverse size obtained is well within our requirements for UEM systems. As pointed out in the previous section, spatial resolution also depends on the transverse emittance, and our data for the UEM column confirms the results of our photoemission simulations (namely, that the cigar-shaped pulse offers a lower emittance than the pancake pulse). Shaping the radial profile of the photoemitting laser pulse to generate an ellipsoidal electron bunch allows to reduce the emittance by a factor of 2, bringing the emittance of the pancake-like pulses within our target range as well.

For time-resolved applications, both the bunch length and energy spread are critical parameters. For pancake-like pulses, the bunch length (calculated from the longitudinal size as $\delta t = 2\sqrt{2\sigma_z}/v_0$) is increased from $\delta t = 13$ fs for the 10^5 electron pulse to $\delta t = 290$ fs for the pulse with 10^7 electrons. The energy spread also increases similarly with the pulse charge. For $N_e = 10^6$, these parameters are already within our target range, and further improvement can be obtained by switching to ellipsoidal bunches. On the other hand, while the cigar-like pulse offers good spatial resolution, it is not easily used for time-resolved measurements, as longitudinal focusing to the sizes needed can be challenging due to the length of the pulse.

4. CONCLUSIONS

We have presented our model for simulating the time-dependent evolution of a photoemitted electron pulse and show good agreement with experimental results obtained using the shadow imaging technique. At short timescales, the spatial profile of the emitted electron pulse depends on the laser used to generate it, and the distribution of velocities is indicative of a turbulent flow related to the initial thermal distribution and independent of extraction field, as observed in Figure 2(A). At later times, as the pulse moves away from the surface, its properties display a strong dependence on the extraction conditions: Below the virtual cathode limit, the pulse becomes fully laminar, evolving into the typical ellipsoidal shape, while above the virtual cathode, some turbulent flow is present and the pulse does not fully detach from the surface.

Our investigation of the optimal conditions for pulse generation in terms of laser fluence and extraction field F_a for different experimental realizations

shows evidence of virtual cathode formation as the initial number of electrons is increased as a consequence of space charge effects. We also vary the aspect ratio of the photoemitting laser pulse and show how the emittance, coherence length, and energy spread depend on the number of electrons needed in a single pulse and on the extraction field. Based on the desired resolution, it is possible to find the optimal conditions of pulse generation.

Given these photoemission conditions, we also derive a mean-field formalism to simulate the propagation of an electron pulse through a microscope column. We include a description of the photoemission gun, magnetic lenses, and an RF cavity in our model for the UEM system and give quantitative predictions of the achievable spatial and temporal resolutions both for pancake-like and cigar-like electron pulses. Given the limitations of the analytic Gaussian model, these predictions should be viewed as best-case results since aberrations and deviations of the pulse from the assumed self similar Gaussian profile were neglected. Nevertheless, due to the simplicity of the model and the resulting ease of computation, we believe that our model can offer a valuable tool in understanding the achievable resolution in UEM systems and allow one to search for optimal configurations over a vast range of parameters.

ACKNOWLEDGMENTS

We thank Dr. Zhensheng Tao for the insightful discussion and comments, and we acknowledge support from U.S. National Science Foundation under Grant No. NSF-DMR 1126343 and the U.S. Department of Energy under Grant No. DE-FG02-08ER41546. Computational work in support of this research was performed at Michigan State University High Performance Computing Center.

REFERENCES

Berger, J. A., Hogan, J. T., Greco, M. J., Schroeder, W. A., Nicholls, A. W., & Browning, N. D. (2009). DC photoelectron gun parameters for ultrafast electron microscopy. *Microscopy and Microanalysis, 15*, 298–313.

Berger, J. A., & Schroeder, W. A. (2010). Semianalytic model of electron pulse propagation: Magnetic lenses and RF pulse compression cavities. *Journal of Applied Physics, 108*, 124905.

Berglund, C. N., & Spicer, W. E. (1964). Photoemission studies of copper and silver: Theory. *Physical Review, 136*, A1030–A1044.

Carbone, F., Musumeci, P., Luiten, O., & Hebert, C. (2012). A perspective on novel sources of ultrashort electron and x-ray pulses. *Chemical Physics, 392*, 1–9.

Dowell, D. H., & Schmerge, J. F. (2009). Quantum efficiency and thermal emittance of metal photocathodes. *Physical Review Special Topics—Accelerators and Beams, 12*, 074201.

Filippetto, D., Musumeci, P., Zolotorev, M., & Stupakov, G. (2014). Maximum current density and beam brightness achievable by laser-driven electron sources. *Physical Review Special Topics—Accelerators and Beams, 17*, 024201.

Hau-Riege, S. P., Graf, A., Doeppner, T., London, R. A., Krzywinski, J., Fortmann, C., et al. (2012). Ultrafast transitions from solid to liquid and plasma states of graphite induced by x-ray free-electron laser pulses. *Physical Review Letters, 108*, 217402.

King, W. E., Campbell, G. H., Frank, A., Reed, B., Schmerge, J. F., Siwick, B. J., et al. (2005). Ultrafast electron microscopy in materials science, biology, and chemistry. *Journal of Applied Physics, 97*, 111101.

Li, R. K., & Musumeci, P. (2014). Single-shot MeV transmission electron microscopy with picosecond temporal resolution. *Physical Review Applied 2*, 024003.

Luiten, O., van der Geer, S., de Loos, M., Kiewiet, F., & van der Wiel, M. (2004). How to realize uniform three-dimensional ellipsoidal electron bunches. *Physical Review Letters, 93*.

Makino, K., & Berz, M. (2006). COSY INFINITY version 9. *Nuclear Instruments and Methods in Physics Research Section A, 558*, 346–350.

Michalik, A. M., & Sipe, J. E. (2006). Analytic model of electron pulse propagation in ultrafast electron diffraction experiments. *Journal of Applied Physics, 99*, 054908.

Nicodemus, R. A., Corcelli, S. A., Skinner, J. L., & Tokmakoff, A. (2011). Collective hydrogen bond reorganization in water studied with temperature-dependent ultrafast infrared spectroscopy. *Journal of Physical Chemistry B, 115*(18), 5604–5616.

Portman, J. (2014). Ultrafast science: A multiscale modeling approach to femtosecond electron diffraction and its applications. Ph.D. thesis, Michigan State University, East Lansing.

Portman, J., Zhang, H., Makino, K., Ruan, C.-Y., Berz, M., & Duxbury, P. M. (2014). Untangling the contributions of image charge and laser profile for optimal photoemission of high-brightness electron beams. *Journal of Applied Physics, 116*, 174302.

Portman, J., Zhang, H., Tao, Z., Makino, K., Berz, M., Duxbury, P. M., & Ruan, C.-Y. (2013). Computational and experimental characterization of high-brightness beams for femtosecond electron imaging and spectroscopy. *Applied Physics Letters, 103*, 253115.

Ruan, C.-Y., Murooka, Y., Raman, R. K., Murdick, R. A., Worhatch, R. J., & Pell, A. (2009). The development and applications of ultrafast electron nanocrystallography. *Microscopy and Microanalysis, 15*(4), 323–337.

Ruan, C.-Y., Vigliotti, F., Lobastov, V. A., Chen, S., & Zewail, A. H. (2004). Ultrafast electron crystallography: Transient structures of molecules, surfaces, and phase transitions. *Proceedings of the National Academy of Sciences USA, 101*(5), 1123–1128.

Tao, Z., Han, T., Mahanti, S., Duxbury, P., Yuan, F., Ruan, C.-Y., et al. (2012a). Decoupling of structural and electronic phase transitions in VO_2. *Physical Review Letters, 109*, 166406.

Tao, Z., Zhang, H., Duxbury, P. M., Berz, M., & Ruan, C.-Y. (2012). Space charge effects in ultrafast electron diffraction and imaging. *Journal of Applied Physics, 111*(4), 044316.

Valfells, A., Feldman, D. W., Virgo, M., O'Shea, P. G., & Lau, Y. Y. (2002). Effects of pulse-length and emitter area on virtual cathode formation in electron guns. *Physics of Plasmas, 9*, 2377–2382.

van der Geer, S., de Loos, M., Vredenbregt, E., & Luiten, O. (2009). Ultracold electron source for single-shot, ultrafast electron diffraction. *Microscopy and Microanalysis, 15*, 282–289.

van Oudheusden, T., de Jong, E. F., van der Geer, S. B., Root, W. P. E. M. O., Luiten, O. J., & Siwick, B. J. (2007). Electron source concept for single-shot sub-100-fs electron diffraction in the 100-keV range. *Journal of Applied Physics, 102*, 093501.

van Oudheusden, T., Pasmans, P. L. E. M., van der Geer, S. B., de Loos, M. J., van der Wiel, M. J., & Luiten, O. J. (2010). Compression of subrelativistic space-charge-dominated electron bunches for single-shot femtosecond electron diffraction. *Physical Review Letters, 105*, 264801.

Zewail, A. H. (2000). Femtochemistry: Atomic-scale dynamics of the chemical bond. *Journal of Physical Chemistry A, 104*, 5660–5694.
Zewail, A. H. (2010). Four-dimensional electron microscopy. *Science, 328*(5975), 187–193.
Zhang, H. (2013). The fast multipole method in the differential algebra framework for the calculation of 3D space charge fields. Ph.D thesis, Michigan State University, East Lansing.
Zhang, H., & Berz, M. (2011). The fast multipole method in the differential algebra framework. *Nuclear Instruments and Methods in Physics Research Section A, 645*, 338–344.
Zhang, H., Tao, Z., Ruan, C.-Y., & Berz, M. (2015). Space charge simulations of photoemission using the differential algebra-based multiple-level fast multipole algorithm. In *Proceedings of the Conference on Femtosecond Electron Imaging and Spectroscopy, FEIS 2013*. 56–66.